Matter

CellPress
OPEN ACCESS

Article

Multigenerational Crumpling of 2D Materials for Anticounterfeiting Patterns with Deep Learning Authentication

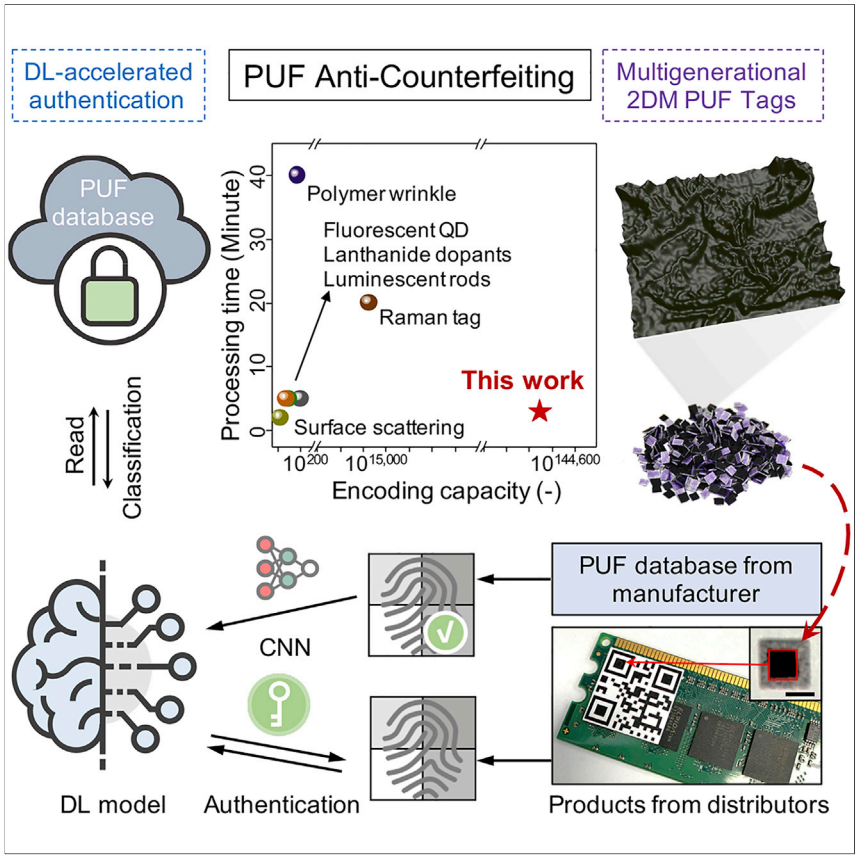

Multigenerational 2D-material (2DM) microstructures are fabricated via sequential deformations in a transfer-free fashion and exhibit physical unclonable function patterns with algorithm-recognizable features. Deep learning (DL)-facilitated software is developed on the basis of the "classification and validation" mechanism to shorten the authentication time. With 2DM tags and DL software, a reliable and environmentally stable anticounterfeiting technology, *DeepKey*, is realized to show superior encoding capacity and fast authentication, which can be applied as an add-on covert layer for QR codes to provide two-layer information security.

Demonstrate
Proof-of-concept of performance with intended application/response

Lin Jing, Qian Xie, Hongling Li, ..., Edwin Hang Tong Teo, Xiaonan Wang, Po-Yen Chen

chewxia@nus.edu.sg (X.W.)
checp@umd.edu (P.-Y.C.)

HIGHLIGHTS

Multiscale 2D-material microstructures are fabricated via sequential deformations

Multigenerational 2D-material microstructures serve as PUF key-based patterns

DL-facilitated software is developed to accelerate authentication

DeepKey anticounterfeiting features high encoding capacity and fast authentication

Jing et al., Matter 3, 2160–2180
December 2, 2020
Published by Elsevier Inc.
https://doi.org/10.1016/j.matt.2020.10.005

CellPress
OPEN ACCESS

Matter

Article

Multigenerational Crumpling of 2D Materials for Anticounterfeiting Patterns with Deep Learning Authentication

Lin Jing,[1,4] Qian Xie,[2,4] Hongling Li,[3] Kerui Li,[1] Haitao Yang,[1] Patricia Li Ping Ng,[1] Shuo Li,[1] Yang Li,[1] Edwin Hang Tong Teo,[3] Xiaonan Wang,[1,*] and Po-Yen Chen[1,5,*]

SUMMARY

Physical unclonable function (PUF) is a cornerstone of anticounterfeiting. However, conventional PUF key-based secure tags encounter several bottlenecks, such as complicated manufacturing, specialized and tedious readout, long authentication time, and insufficient stability. Here, we utilize various two-dimensional materials (2DMs), including $Ti_3C_2T_x$ MXene and graphene oxide, to construct multigenerational microstructures as PUF patterns. Two intermediate treatments, cation intercalation and moisture-induced lubrication, are introduced in between sequential contractions to engineer the multiscale patterns in a transfer-free and scalable fashion. A deep learning (DL)-facilitated software is developed to pre-categorize the hierarchical topographies with classifiable features. Thereafter, the search-and-compare is conducted within a smaller database to shorten the overall authentication time. The synergy between 2DM tags and DL-facilitated software enables a reliable and environmentally stable anticounterfeiting technology, *DeepKey*, showing superior encoding capacity ($>10^{144,494}$) and short authentication time (~3.5 min). Our 2DM anticounterfeiting tag is finally integrated with QR codes to provide two-layer information security.

INTRODUCTION

Physical unclonable function (PUF), possessing unique physical manifestations with sufficient complexity, is one of the cornerstones of highly secure anticounterfeiting technologies.[1] PUF refers to the physical object with inherent, distinct, and fingerprint-like features, which is fundamentally secure. In principle, unique PUF patterns are generated in a stochastic and nondeterministic fashion and can provide huge encoding capacity (i.e., theoretical maximum number of distinct PUF patterns), making them nearly impossible to be repeated or reproduced. Conventional approaches to achieving PUF secure keys for anticounterfeiting usually involve solution chemistry affording large parameter space and high randomness[2–4] or construction of complex electronic systems with diverse disorders and inherent defects.[5,6] Most of these approaches require additional taggants for readout purposes (e.g., stimulated luminescence,[7,8] surface-enhanced Raman scattering[9]) and/or delicate device fabrication (e.g., microtransistors[5,6]). In addition, the readout processes of current PUF systems (e.g., spectrum verification,[10,11] current profile measurement,[5,6] minutiae extraction[3]) require specialized equipment setups, and the necessity of conducting one-by-one search-and-compare algorithms within huge databases further makes the overall authentication time consuming.[1,3,12,13] Another technical challenge of

Progress and Potential

Physical unclonable function (PUF) is a cornerstone of anticounterfeiting, yet conventional PUF key-based tags encounter several bottlenecks, such as complicated manufacturing, specialized and tedious readout, long authentication time, and insufficient environmental stability. Here, we utilize two-dimensional materials (2DMs) to construct multigenerational microstructures as PUF patterns. By implementing two *in situ* treatments during sequential substrate contractions, multigenerational 2DM PUF patterns are produced in a transfer-free and scalable fashion. A deep learning (DL)-facilitated authentication software is further developed on the basis of the "classification and validation" mechanism, shortening the authentication time significantly. The synergy between 2DM tags and DL authentication software enables a *DeepKey* anticounterfeiting technology with superior encoding capacity and fast authentication, which can be integrated with QR codes to provide two-layer information security.

CellPress
OPEN ACCESS

current PUF tags is their insufficient environmental stability against light,[7,14] heat,[15,16] and physical stress,[11,17] which restrict their long-term anticounterfeiting exploitation.

Complex out-of-plane topographies emerge in the ultrathin two-dimensional material (2DM) layers attached to elastomeric substrates under in-plane contractions. Owing to the unpredictable interfacial deformations at micro-/nanoscale,[18–20] the resulting 2DM topographies (e.g., wrinkles, crumples) exhibit random and unclonable physical micropatterns, which can serve as the PUF secure keys. On top of the PUF nature,[3,21] the excellent physical stability[22] of 2DMs makes these patterns competitive candidates for stable anticounterfeiting tags.[3,23,24] Furthermore, the out-of-plane characteristics of 2DM microstructures can be programmably designed across multiple length scales, producing various hierarchical topographies.[18,19,24–26] The combination of multiscale features with specific orientations can serve as unique identifiers to classify and categorize the resulting 2DM hierarchies into specific subgroups. With the pre-categorization step, the search-and-compare algorithm only needs to be conducted within a smaller database, thus shortening the overall authentication time. To realize this concept of accelerated authentication, a facile and scalable approach to fabricating 2DM PUF secure keys with classifiable features becomes essential. Several sequential deformation strategies have been investigated in the literature to enable the sophisticated design of hierarchical 2DM topographies.[18,25,26] However, the majority of reported methods involved repeated substrate dissolution and/or delicate 2DM film transfer, severely limiting the scalability of pattern fabrication and the capability of topographic tuning.

In this work, we adopted both graphene oxide (GO) and titanium carbide ($Ti_3C_2T_x$) MXene to construct multigenerational microstructures as PUF key-based anticounterfeiting patterns. Two intermediate treatments, cation intercalation (CI) and moisture-induced lubrication (MIL), were implemented in between sequential balloon deflations to *in situ* engineer the multiscale topographies of 2DMs in a transfer-free and scalable fashion (Figures 1A and S1). With both CI and MIL treatments, multigenerational GO and MXene structures (22 types in total) were produced by the pre-determined deflation programs without the need of substrate removal or film transfer. The multigenerational 2DM hierarchies were then utilized as PUF key-based tags for anticounterfeiting applications (Figure 1B). To accelerate the authentication process of these 2DM tags, we developed a deep learning (DL)-facilitated software to categorize the hierarchical topographies with classifiable features, after which we conducted a search-and-compare algorithm only within the narrowed database to shorten the validation time. With classifiable 2DM anticounterfeiting patterns and DL-facilitated authentication software, a reliable (zero "false-positive" case for the database of 1,760 patterns) and environmentally stable anticounterfeiting technology, *DeepKey*, was developed, demonstrating superior encoding capacity ($>10^{144,494}$) and short authentication time (~3.5 min for readout plus authentication) in comparison with the state-of-the-art PUF-based anticounterfeiting systems. In *DeepKey*, the 2DM anticounterfeiting tag can serve as an add-on covert layer for traditional QR codes to provide two-layer information security.

RESULTS AND DISCUSSION

Intermediate CI Treatment Produces Hierarchical GO Topographies

The intermediate CI step was implemented to tune the mechanical mismatch between 2DM layer and elastomeric substrate during sequential deformations.

[1]Department of Chemical and Biomolecular Engineering, National University of Singapore, 4 Engineering Drive, Singapore 117585, Singapore

[2]School of Metallurgic Engineering, Anhui University of Technology, 59 Hudong Road, Ma'anshan 243002, P.R. China

[3]School of Electrical and Electronic Engineering, Nanyang Technological University, 50 Nanyang Avenue, Singapore 639798, Singapore

[4]These authors contributed equally

[5]Lead Contact

*Correspondence: chewxia@nus.edu.sg (X.W.), checp@umd.edu (P.-Y.C.)

https://doi.org/10.1016/j.matt.2020.10.005

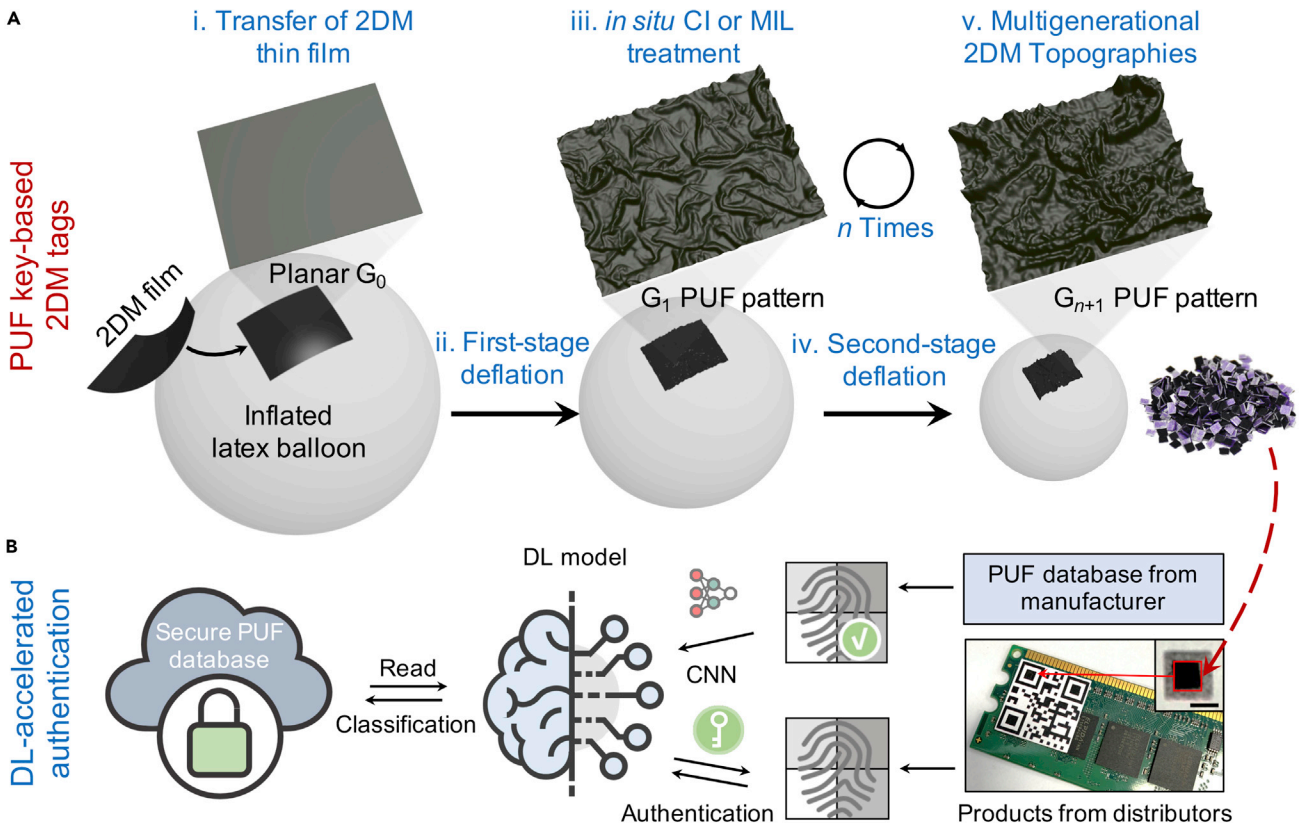

Figure 1. Hierarchical Two-Dimensional Material (2DM) Topographies with Classifiable Physically Unclonable Functions (PUFs) for Deep Learning (DL)-Facilitated Anticounterfeiting

(A) Schematic illustration of transfer-free fabrication of multigenerational 2DM topographies, which included the following steps: (i) transfer of planar generation 0 (G_0) 2DM thin film onto an inflated latex balloon, (ii) first-stage balloon deflation, (iii) intermediate cation intercalation (CI) treatment to adjust mechanical mismatch or intermediate moisture induced lubrication (MIL) treatment to tune interfacial adhesion energy, and (iv) second-stage deflation. Steps (iii) and (iv) can be repeated *n* times to achieve (v) multigenerational G_{n+1} 2DM topographies. Inset is the photo showing ~300 pieces of MXene PUF tags produced through scalable fabrication.

(B) G_{n+1} 2DM topographies with classifiable PUF patterns for anticounterfeiting technology development. High-level characteristics of PUF patterns were recognized by convolutional neural network (CNN) DL algorithms, enabling the development of an efficient two-step authentication mechanism consisting of classification and validation, demonstrated by our self-developed *DeepKey* authentication software. Scale bar, 2 mm.

The classic equation for wrinkles generated in a thin film compliantly bonded to an elastomeric substrate is shown in Equation 1,[27]

$$\lambda = 2\pi h(\overline{E}_f/3\overline{E}_s)^{1/3}, \qquad \text{(Equation 1)}$$

where λ is the characteristic wavelength of wrinkle, h is the thickness of film, and E_f and E_s stand for the Young's moduli of top-layer film (f) and bottom-layer substrate (s), respectively; $\overline{E} = E/(1-v^2)$, where v is the Poisson's ratio. A simple strategy to tune the wrinkle wavelength is through adjusting the Young's modulus of the top 2DM layer to control the mechanical mismatch at the 2DM/elastomer interface. Several methods to increase the Young's modulus of the top 2DM layer include (1) increasing the lateral size of 2DM nanosheets,[28] (2) introducing more functional groups onto 2DM nanosheets,[29] and (3) intercalating metal ions[30] into 2DM multilayers,[31,32] where only approach (3) can be conducted in an *in situ* fashion and was adopted here. It is noted that the Young's modulus of a GO film, after overnight immersion in $Al(NO_3)_3$ solution, increased from 0.99 (neat GO) to 3.39 GPa (Al^{3+}-intercalated GO, 1.26 atom % [atomic ratio], abbreviated as Al-GO), while the modulus of

CellPress
OPEN ACCESS

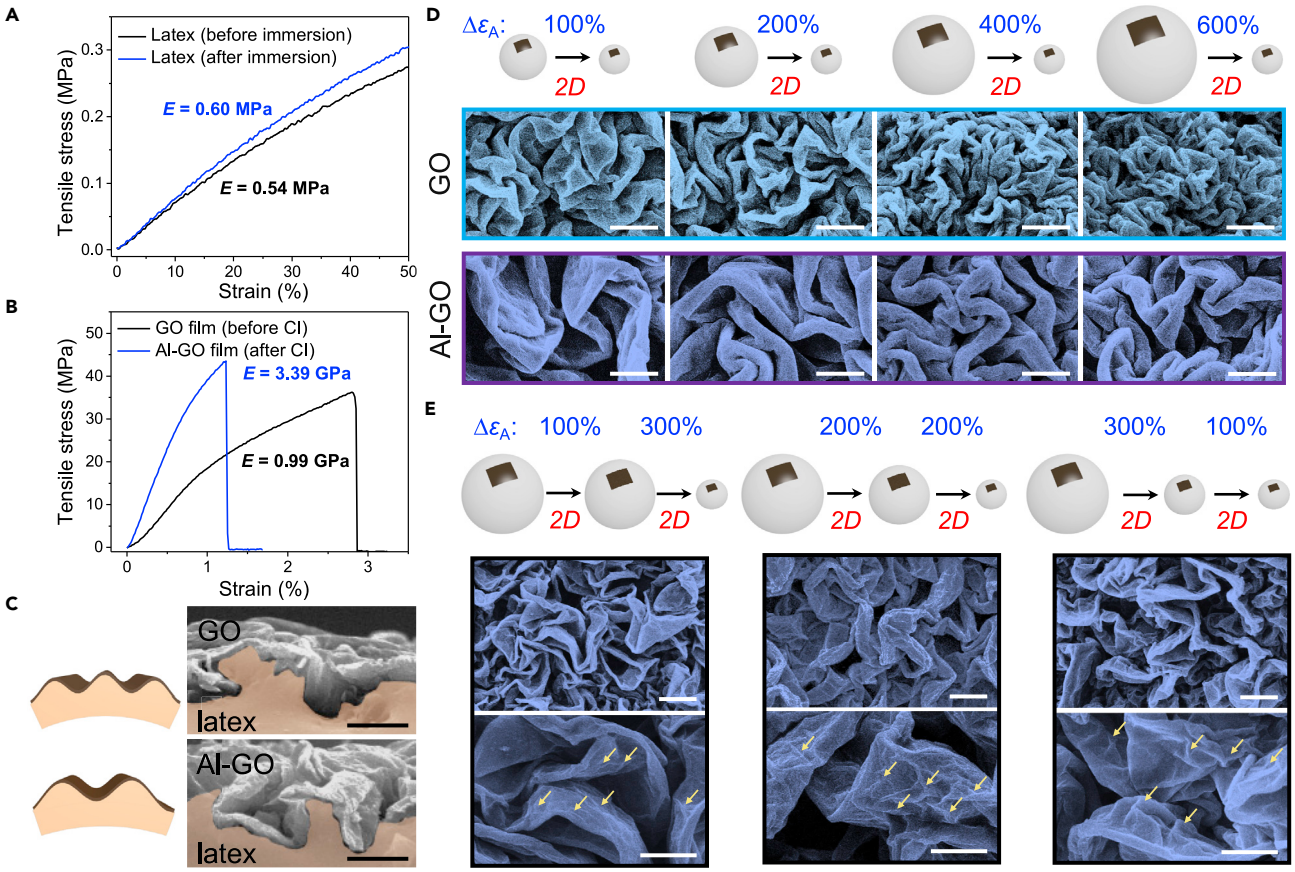

Figure 2. Cation Intercalation Treatment for Creation of Hierarchical Graphene Oxide Topographies by Adjusting Interfacial Mechanical Mismatch

(A and B) Stress-strain curves of latex substrates (A) and graphene oxide (GO) thin films (B) before and after overnight immersion in 0.1 M $Al(NO_3)_3$ solution.

(C) Schematic illustration and corresponding cross-sectional SEM images of GO/latex and Al^{3+}-intercalated GO (Al-GO)/latex bilayer structures after the areal strain (ε_A) release, where the conformal and interlocked interfaces were observed for both structures. Scale bar, 5 μm.

(D) Top-view SEM images of generation 1 isotropic (G_1/*2D*) GO and G_1/*2D* Al-GO crumples generated under the ε_A of 100%, 200%, 400%, and 600%, exhibiting the GO crumple sizes decreasing from ~15 × 15, 10 × 10, 6 × 6, to 4 × 4 μm, which were respectively smaller than the Al-GO crumple sizes varying from ~30 × 30, 20 × 20, 10 × 10, to 6 × 6 μm. Scale bar, 10 μm.

(E) Top-view SEM images of hierarchical G_2/*2D*-*2D* topographies fabricated by sequential deflations of GO-coated balloon with intermediate cation intercalation treatment. The feature sizes of both G_1 and G_2 crumples were finely tuned by controlling the areal strain released ($\Delta\varepsilon_A$) at each deflation stage. As representatives, for two-stage deflations of 100%–300%, 200%–200%, and 300%–100% (denoted as $\Delta\varepsilon_A$ at first stage–$\Delta\varepsilon_A$ at second stage), the G_1 crumple size varied from ~3 × 3, 6 × 6, to 10 × 10 μm and the G_2 crumple size varied from ~20 × 20, 30 × 30, to 40 × 40 μm, respectively. Scale bars, 20 (top row) μm and 10 μm (bottom row).

latex substrate remained unchanged at ~0.6 MPa (Figures 2A and 2B). To visualize the CI effect on the GO topographies under large deformation, we first transferred a 500-nm-thick, planar GO film (generation 0, G_0) onto an inflated latex balloon (characterizations of GO nanosheets and multilayers are presented in Figures S2A–S2C). The conformal adhesion of GO nanocoating was enabled by the pre-treatment of oxygen plasma of latex balloon, which generated hydroxyl groups on the elastomeric surface and induced hydrogen bonding with the top GO layer. The GO-coated inflated balloon then underwent overnight Al^{3+} intercalation followed by one-step isotropic (*2D*) deflation to produce G_1/*2D* Al-GO crumple structures. For comparison, G_1/*2D* GO crumple structures were also fabricated for comparison. Both Al-GO/latex and GO/latex structures exhibited extended and interlocked interfaces (Figure 2C), indicating that they followed the same deformation mode of conformal

wrinkling. Because of the rigidification of the top GO layer via Al^{3+} intercalation (larger mismatch with latex), the sizes of G_1/*2D* Al-GO crumples were much larger than the G_1/*2D* GO ones under the same degree of contraction (Figure 2D); the definition and quantification of crumple size are detailed in Figure S3A.

To generate hierarchical GO topographies, we conducted sequential deflations of GO-coated balloon and implemented the intermediate CI treatment. For instance, a G_0 GO film was transferred onto an inflated latex balloon followed by first-stage deflation. The partially deflated GO-coated balloon then underwent CI treatment to increase the Young's modulus of the top 2DM layer. After second-stage (full) deflation, hierarchical Al-GO structures (G_2/*2D-2D*) composed of small G_1 crumples (from first-stage deflation) on top of large G_2 crumples (from second-stage deflation) were observed (Figure 2E). Without intermediate CI treatment, no hierarchical characteristic was obtained after multistage deflations (Figures S4A and S4B). In addition, by modulating the areal strain (ε_A) released at each deflation stage, the characteristic features were precisely tuned at different length scales. By programming the areal strains of sequential deflations ([$\Delta\varepsilon_A$ at first stage] to [$\Delta\varepsilon_A$ at second stage]), the G_2/*2D-2D* GO hierarchies that followed the deflation programs of 300%–100%, 200%–200%, and 100%–300% exhibited the G_1 crumples sizing from ~3 × 3, 6 × 6, to 10 × 10 μm and the G_2 crumples from ~20 × 20, 30 × 30, to 40 × 40 μm, respectively (Figure S3B). Both G_1 and G_2 feature sizes can be further tuned upon specific requests by simply adjusting the $\Delta\varepsilon_A$ at each deflation stage, demonstrating dominant advantages over conventional multistep methods with fixed pre-strain for each deformation.[18,24,26] Moreover, the intercalated Al^{3+} ions within as-deformed Al-GO topographies were able to be completely rinsed out by dilute HCl solution (Figures S2E–S2G). The intermediate CI treatment is specifically suitable for the 2DM units that can be strongly crosslinked with metal ions, such as GO. Nevertheless, for other 2DMs such as MXene, the CI effect was insignificant. Therefore, a more generalized method is highly needed to expand the selection of available 2DM candidates, which can endow add-on functions to the anticounterfeiting tags or can be applied to other applications.[18,33–35]

Intermediate MIL Treatment Creates Hierarchical MXene Topographies

Another critical factor that can be tuned is the interfacial adhesion energy (*G*) between the top 2DM layer and bottom latex substrate.[36] When the *G* of 2DM layer on latex is lower than the critical adhesion energy (G_C) calculated by Equation 2,[36–39]

$$G_C = \varepsilon^2 E_f h, \qquad \text{(Equation 2)}$$

where ε is the uniaxial strain, the formation of delaminated large buckles is energetically preferred over conformal wrinkling upon the strain release. Inspired by this, an intermediate MIL treatment was implemented between consecutive deflation stages by introducing moisture as a benign lubricant, which attenuates the *G* of 2DM/latex interface to be lower than G_C.[40,41] After the MIL treatment, the deformation mode can be intentionally transitioned from conformal wrinkling to delaminated buckling. MXene was chosen as the representative 2DM for the MIL treatment. The preparation and characterization of MXene nanosheets are presented in Figures S5A–S5F. Similarly, a 500-nm-thick MXene film was first transferred onto an inflated latex balloon, where the adhesion between MXene film and latex was enhanced by the pre-treatment of oxygen plasma on latex. To introduce the moisture lubricant, we kept the MXene-coated inflated balloon at 4°C overnight and then exposed it to room temperature (25°C, at the relative humidity [RH] of 68%) to condense the moisture layer at MXene/latex interface. The mechanical properties of MXene and latex were well retained after the MIL treatment (Figures S6A and S6B). On the other hand,

CellPress
OPEN ACCESS

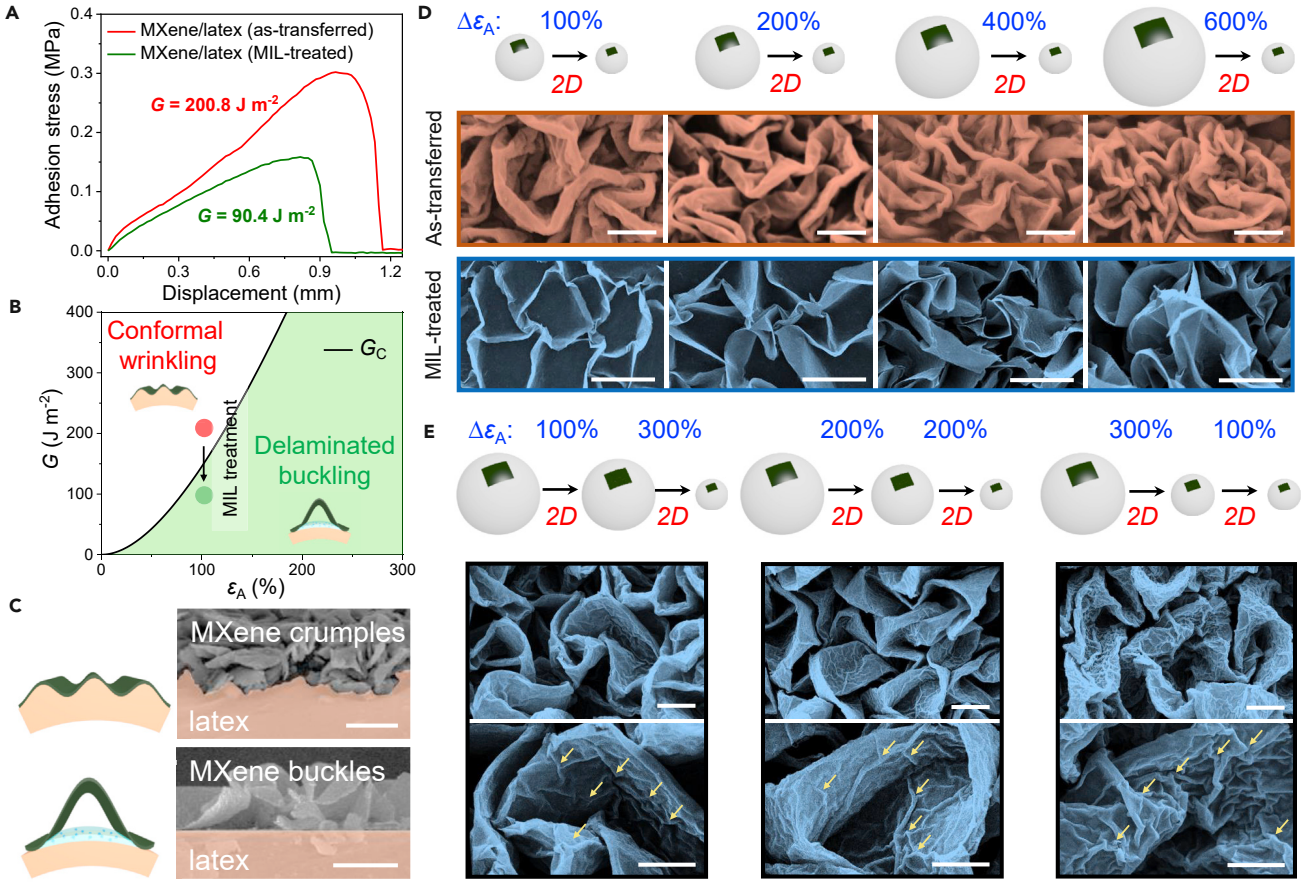

Figure 3. Moisture-Induced Lubrication Treatment for Creation of Hierarchical MXene Topographies through Transitioning Deformation Mechanism from Conformal Wrinkling to Delaminated Buckling

(A) Delamination tests of MXene/latex interface before and after moisture-induced lubrication (MIL) treatment.

(B) Adhesion energy decreased from 200.8 to 90.4 J m^{-2} after MIL treatment, resulting in the transition of deformation mechanism from conformal wrinkling to delaminated buckling.

(C) Schematic illustration and cross-sectional SEM images of MIL-treated MXene/latex structures confirmed the transition of deformation mechanism, where much larger delaminated buckles were observed after MIL treatment. Scale bars, 5 μm (top) and 50 μm (bottom).

(D) Top-view SEM images of as-transferred G_1/*2D* MXene crumples and G_1/*2D* MIL-induced MXene buckles generated under the ε_A of 100%, 200%, 400%, and 600%, exhibiting the MXene crumple sizes decreasing from ~30 × 30, 20 × 20, 12 × 12, to 6 × 6 μm, which were respectively smaller than the sizes of MIL-induced MXene buckles varying from ~150 × 150, 120 × 120, 80 × 80, to 50 × 50 μm. Scale bars, 10 μm (top row) and 100 μm (bottom row).

(E) Top-view SEM images of hierarchical G_2/*2D*-*2D* topographies fabricated by sequential deflations of MXene-coated balloon with intermediate MIL treatment. The sizes of both G_1 and G_2 crumples were finely tuned by controlling $\Delta\varepsilon_A$ at each deflation stage. As representatives, for two-stage deflations with $\Delta\varepsilon_A$ of 100%–300%, 200%–200%, and 300%–100%, the G_1 crumple sizes varied from ~5 × 5, 8 × 8, to 10 × 10 μm, and the G_2 crumple sizes varied from ~40 × 40, 55 × 55, to 75 × 75 μm, respectively. Scale bars, 20 μm (top row) and 10 μm (bottom row).

the *G* of MXene/latex interface (under ε_A of 100%) before and after the introduction of moisture lubricant was characterized by the delamination tests (Figure 3A, for experimental details see Supplemental Experimental Procedures), where *G* dramatically decreased from 200.8 to 90.4 J m^{-2} (corresponding G_C was 142.9 J m^{-2}), demonstrating the successful transition of deformation mechanism to delaminated buckling (Figure 3B).

To visualize the MIL effect on the MXene topographies under deformation, we fully deflated the MIL-treated MXene-coated balloon to produce a G_1/*2D* MXene/latex structure. After the MIL treatment, the attenuated adhesion energy resulted in the partial delamination of MXene film accompanied by isotropic buckling during latex

contraction, as indicated by the cross-sectional scanning electron microscopy (SEM) image (Figure 3C). Figure 3D shows that the delaminated MXene buckles (treated by MIL) exhibited much larger topographic features than the conformal MXene crumples (without MIL). Similarly, hierarchical MXene topographies were produced by conducting sequential deflations of the MXene-coated balloon with intermediate MIL treatment implemented. A G_0 planar MXene film was first transferred onto an inflated latex balloon followed by first-stage deflation. The partially deflated MXene-coated balloon subsequently underwent MIL treatment to transition the deformation mode to delaminated buckling. After second-stage (full) deflation, hierarchical MXene structures (G_2/*2D-2D*) with combinative structural characteristics were obtained, where smaller G_1 crumples (from first-stage deflation) were on top of large G_2 buckles (from second-stage deflation). The details regarding quantification of buckle and crumple size are given in Figures S7A and S7B. Without the MIL treatment, no hierarchical characteristic was obtained after multistage deflations (Figures S4C and S4D). Nonetheless, by adjusting the $\Delta\varepsilon_A$ at each deflation step, the sizes of primary buckles and secondary crumples in G_2/*2D-2D* GO hierarchies were able to be programmably controlled (Figure 3E). This MIL approach was proved to be more versatile than the CI treatment, which was also applicable to other 2DMs (e.g., GO, as shown in Figures S8A and S8B). The intermediate CI and MIL treatments can be applied sequentially during the multistage balloon deflations to create multigenerational 2DM hierarchies. It is worth noting that the CI step has to be conducted prior to MIL treatment to ensure conformal attachment of the upper 2DM layer; otherwise, irreversible detachment of the 2DM layer may appear.

To summarize, the characteristic size of topographic patterns of 2DM PUF tags can be adjusted through four approaches, which include varying the pre-strain applied, tuning the mechanical properties or thicknesses of top 2DM thin films, and alternating the deformation mechanism. These approaches can be applied individually or combinatively where applicable.

(1) Adjusting the pre-strain applied. As presented in Figure 2D, under pre-applied areal strains (ε_A) of 600%, 400%, 200%, and 100%, the crumple sizes of GO can be increased from ~4 × 4, 6 × 6, 10 × 10, to 15 × 15 μm, respectively. Similarly, for MXene crumples generated under the ε_A of 600%, 400%, 200%, and 100% (Figure 3D), their sizes can be correspondingly adjusted from ~6 × 6, 12 × 12, 20 × 20, to 30 × 30 μm, respectively. Therefore, if a larger topographic pattern is demanded, one way is to decrease ε_A while producing the crumples or wrinkles.
(2) Adjusting the mechanical properties of top 2DM layers. According to Equation 1, a simple way to tune the crumple or wrinkle sizes is through adjusting the Young's modulus of the top 2DM layer. In this work, we have demonstrated this effect by intercalating metal ions into GO layers. As shown in Figures 2B–2D, with the intercalation of 1.26 atom % Al^{3+}, the Young's modulus of GO thin film increased from 0.99 to 3.39 GPa, resulting in the crumple size increasing from ~15 × 15 to ~30 × 30 μm when ε_A of 100% was applied.
(3) Adjusting the adhesion energy at the 2DM/elastomer interface. As presented in Figures 3A–3D, the deformation mechanism of 2DM/elastomer bilayer can be engineered by MIL treatment, leading to the transition from conformal wrinkling to delaminated buckling. As a result, when ε_A of 100% was applied, the crumple size increased from ~30 × 30 to 150 × 150 μm.
(4) Adjusting the thickness of top 2DM layers. According to Equation 1, the change in the thickness of the top 2DM thin film leads to variation in the size of topographic patterns. As shown in Figures S9A and S9B, under ε_A of

200%, the increase in thickness of the top GO film from 0.5 to 2.5 μm resulted in a crumple size increase from ~10 × 10 to 50 × 50 μm. This approach can be combined with approach (1) to achieve even larger crumples. As shown in Figure S9C, further decreasing the ε_A to 100% for the GO thin film with thickness of 2.5 μm led to a crumple size of ~80 × 80 μm.

Multigenerational 2DM Microstructures Can Be Programmably Fabricated by Sequential Substrate Contractions

Besides the isotropic 2DM crumples fabricated by the deflation of a sphere-shaped balloon, periodic wrinkle textures with certain orientation were created by deflating a tube-shaped balloon (see Figures S10A–S10C for details of orientation and wavelength controls).[42] Through the sequential deflations of sphere- or tube-shaped balloons together with the intermediate modification step(s) (CI and/or MIL), both wrinkle (*1D*) and crumple (*2D*) features were programmed into hierarchical 2DM structures with desired combinations at different length scales. The programmable architecturing of upper 2DM layers enabled the fabrication of multigenerational 2DM structures, starting from planar G_0 nanocoatings to multiscale G_3 topographies. The genealogies of GO and MXene are shown in Figure 4 (12 members for each family tree), and the detailed fabrication processes of each 2DM microstructure can be found in Experimental Procedures.

The multigenerational, multidirectional, and multiscale texturing techniques involved the combination of various fabrication strategies, including (1) the use of sphere- or tube-shaped latex balloons, (2) the programmable deflation sequences, and (3) the intermediate CI and/or MIL treatment(s) implemented between consecutive stages of deflations. This programmable architecturing of upper GO and MXene layers rendered rich libraries containing diverse surface textures with disordered yet classifiable topographic characteristics varying from G_0, G_1/*1D*, G_1/*2D*, G_2/*2D-2D*, G_2/*2D-1D*. G_2/*1D-2D*, G_2/*1D*⊥*1D*, G_3/*2D-2D-2D*, G_3/*2D-1D-2D*, G_3/*2D-1D*⊥*1D*, G_3/*1D*||*1D-2D*, G_3/*1D-2D-1D*, G_3/*2D-2D-1D*, to G_3/*1D-2D-2D*, and so forth, which were named after the certain deflation programs applied. The connection line between two topographies in different generations represents one of four deformation orientations, namely *1D*(||) deflation of a tube balloon parallel to its axis, *1D*(⊥) deflation of a tube balloon perpendicular to its axis, and *2D* deflation of a sphere- or a tube-shaped balloon. In the family tree of GO topographies, either CI or MIL treatment can be implemented between two *2D* deflations to fabricate a G_2 structure. To achieve multiscale G_3 GO structures, we applied either two sequential MIL treatments (at 4°C and −80°C subsequently) or sequential CI-MIL treatments during the three-stage deflations. For the genealogy of MXene topographies, the MXene-coated balloons underwent one MIL treatment (at 4°C) and two sequential MIL treatments (at 4°C and −80°C subsequently) to obtain G_2 and G_3 architectures, respectively.

Based on the genealogies of 2DM topographies and the corresponding fabrication procedures, several general trends can be summarized as future design principles. First, the characteristic feature and orientational (dis)order are dependent on the sequence of balloon deflations, that is, the deflation steps do not provide commutative results due to the plastic deformations of 2DM layer. Second, the largest topographic feature is determined by the final deformation mode, whereby the previous series of deformations generated smaller features decorated on top of the largest feature. Third, the characteristic feature size increased with the increasing deflation stages applied, which could be due to the fact that the 2DM nanocoating underwent effective increases in thickness and stiffness while generating the out-of-plane

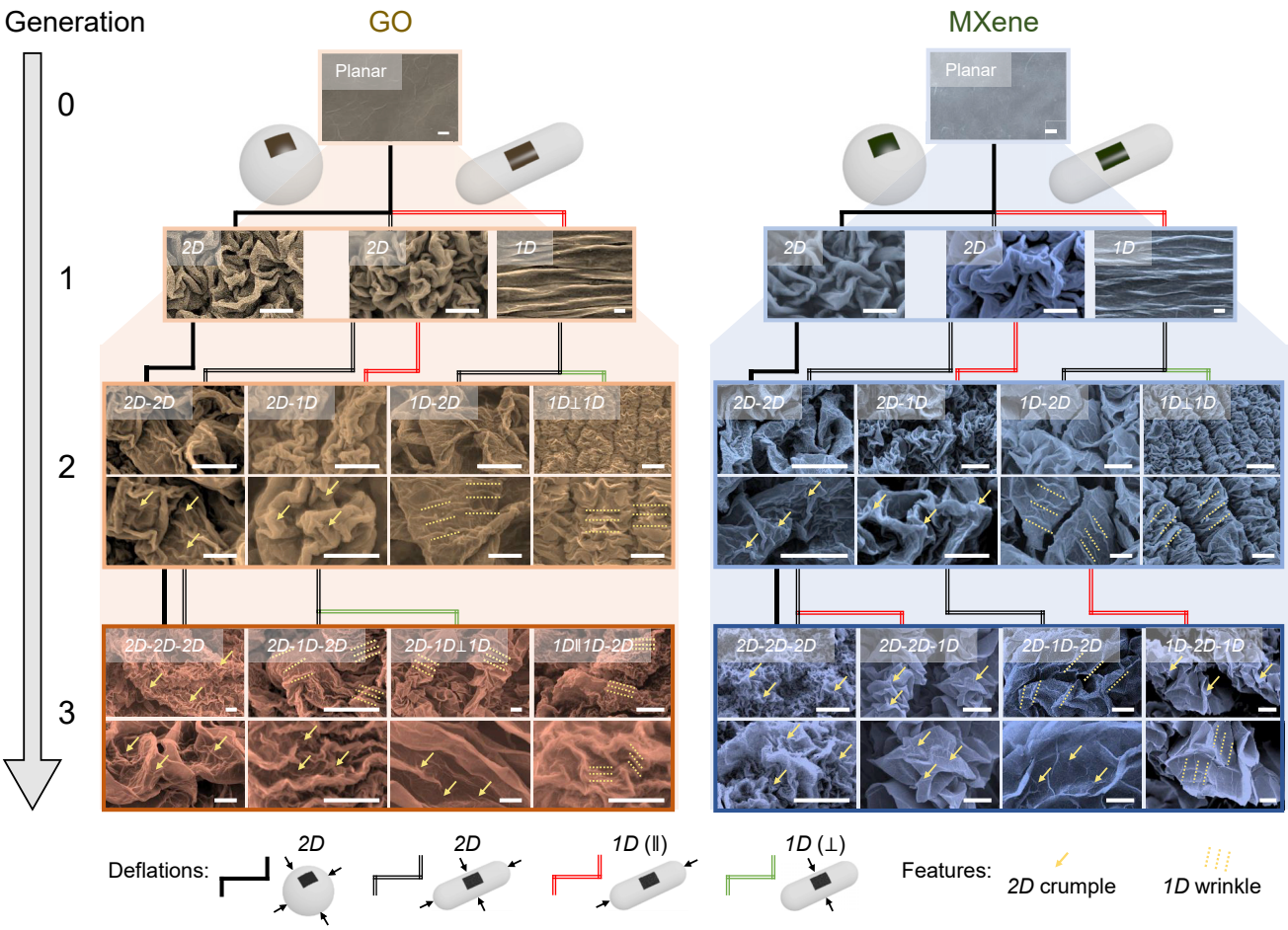

Figure 4. Programmable Architecturing of Multigenerational Two-Dimensional Material Topographies

Genealogies of GO and MXene structures from planar G_0 nanocoating to multiscale G_3 hierarchies, where *1D* wrinkle or *2D* crumple features are programmably encoded at each generation. Colored connection lines represent the deformation types applied, where simple black line stands for the typical *2D* deflation of a sphere-shaped balloon, and double lines with black, red, and green colors stand for *2D*, parallel *1D* (*1D*(∥)), and vertical *1D* (*1D*(⊥)) deflations of a tube-shaped balloon, respectively. Golden arrows and parallel lines stand for features of *2D* crumples and *1D* wrinkles, respectively. Scale bars for GO genealogy from top to bottom, 1 μm (G_0), 10 μm (G_1), 20 μm and 10 μm (G_2), and 50 μm and 10 μm (G_3). Scale bars for MXene genealogy from top to bottom, 1 μm (G_0), 10 μm (G_1), 50 μm and 20 μm (G_2), and 100 μm and 50 μm (G_3).

topographies, leading to the formation of features with larger sizes in the subsequent generation. For example, the crumple sizes of G_3/*2D-2D-2D* GO architecture generated at G_1, G_2, and G_3 increased from ~10 × 10, to 30 × 30, to 100 × 100 μm, respectively. Finally, both MXene and GO families could be further expanded by either increasing the generation numbers or adjusting the $\Delta\varepsilon_A/\Delta\varepsilon$ at each deflation step, whereby the hierarchical structures were able to be finely tuned at different length scales, promising excellent capability of constructing diverse topographies with theoretically unlimited complexity. These principles could lead to a comprehensive and general design strategy for engineering various nanomaterials toward the creation of hierarchical architectures with varying complexity levels, feature size/type, and sequences.

Complex 2DM Patterns Demonstrate High Environmental Stability

As the tag stability is a continual challenge for current PUF systems, we further examined the environmental stability of G_1/*2D* GO and MXene microstructures under multiple simulated conditions. As shown in Figures S11–S13, the GO and MXene

topographies remained intact upon exposure to low (−20°C) and high temperatures (150°C), 0% and 90% RH conditions, organic solvent (dichloromethane), UV light, and long-term daylight. In addition, the $G_1/2D$ MXene patterns exhibited higher stability in acidic and alkaline solutions, where the microstructures were preserved after immersion in 6.0 M HCl and NaOH. Specific details regarding environmental stability tests can be found in Experimental Procedures. We can summarize that these 2DM topographies possess excellent environmental stability upon exposure to various conditions in comparison with most current PUF systems that are vulnerable to light,[7,14] heat,[15,16] and physical stress.[11,17] Also, the material costs of 2 × 2 mm^2-sized MXene and GO tags were estimated to be ca, US$0.0020 each (Supplemental Experimental Procedures), showing their economic feasibility and readiness to be integrated into various products without largely increasing the final costs. It should be noted that our scalable fabrication process barely used specialized equipment and required only conventional equipment without modifications (e.g., vacuum filtration setup, plasma cleaner, fridge). Meanwhile, the superior structure complexity of our 2DM topographies rendered high difficulties in copying their fine details using a typical molding method (Figure S14). These specialties of 2DM hierarchies make them competitive candidates as PUF key-based tags for anticounterfeiting.

DL Model Facilitates Two-Step Authentication of 2DM Patterns

By harnessing the surface instability of balloon deflations, the multigenerational GO and MXene topographies were intrinsically disordered,[3] which were then applied as the PUF key-based anticounterfeiting patterns. The topographic uniqueness of 2DM anticounterfeiting patterns were examined by comparing their SEM images with each other and calculating the corresponding structural similarity index (SSIM)[43] (see detailed calculation in Supplemental Experimental Procedures). As shown in the SSIM map of 296 randomly selected SEM images (across G_1 to G_3, in Figures S15 and S16), each 2DM microstructure presented a unique PUF pattern and was able to serve as an anticounterfeiting pattern with high security. As the conventional methods for pattern recognitions (e.g., visual inspection,[44] minutiae extraction[3]) were not able to fully utilize the rich structural details of 2DM PUF patterns, the authentication in this work was based on comparing the structural information encoded into every pixel of their extracted SEM images. In this case, each single pixel was taken as a unit with varying colors (i.e., grayscale intensity). As such, the information change of any pixel within an individual image may affect its structural similarity and thus affect the SSIM value. As the 2DM PUF patterns are produced in an intrinsically stochastic crumpling/wrinkling fashion, they are anticipated to exhibit an unlimited number of different topographies, leading to all of the pixels being utilized as variables by exhibiting different grayscale levels. A superior encoding capacity of $256^{60,000}$ ($\sim 10^{144,494}$) was estimated for our 2DM anticounterfeiting tag with a resolution of 300 pixels at 256 grayscale intensities (see calculation details in Supplemental Experimental Procedures), which is far higher than those of other state-of-the-art PUF systems (up to $3 \times 10^{15,051}$).[3,7,11,45–48]

Another advantage of applying these 2DM patterns for anticounterfeiting was their classifiable characteristics (e.g., level of structural complexity, type/sequence of deformations, size of topographic features). As shown in Figure S17, the characteristics of 2DM patterns from five different groups (296 patterns in $G_1/1D$, $G_1/2D$, $G_2/1D \perp 1D$, $G_2/2D\text{-}2D$, and $G_3/2D\text{-}2D\text{-}2D$) were extracted and presented in a t-distributed stochastic neighbor embedding (t-SNE) scatterplot (see details in Supplemental Experimental Procedures).[49–51] The t-SNE analysis indicated that these 2DM PUF patterns possess high intra-category homogeneity yet high inter-category heterogeneity, which was recognizable to the rapidly evolving DL algorithms.[7,52] By

taking advantage of the algorithm-recognizable features of these 2DM PUF patterns, a two-step authentication mechanism consisting of classification (Step I) and validation (Step II) was developed to reduce the overall authentication time (Figure 5A). At Step I, the topographical features of the test PUF pattern were first checked by a trained DL model to determine whether it was classified into any category within the database. If the classification result is a FALSE (not matched to any), the test pattern will be considered as FAKE directly. On the other hand, if the result is a TRUE (matched to one of the categories within the database), the test pattern will be sent for subsequent pattern validation. At Step II, a direct search-and-compare algorithm is carried out only within the database of a specific subgroup to validate the PUF pattern. If the validation result is a FALSE (not matched to any), the PUF pattern will be concluded as FAKE; if the result is a TRUE (matched to one of the PUF patterns within the subgroup), the test pattern will be finally confirmed to be REAL.

The DL classification model was trained in a progressive strategy. In short, we took 296 representative high-quality (HQ, Figure S16) SEM images and their low-quality counterparts (LQ, with algorithm-induced variations, Figure S18) from five different categories, which were first input into a convolutional neural network (CNN; for details see Figure S19 and Experimental Procedures).[53] Thereafter, to further cultivate the classification capabilities of DL model, we continued to input multiple SEM images taken under various practical scenarios (1,168 in total, Figure S20) into the CNN. After this progressive training, the DL-enabled model was able to classify the $G_1/1D$, $G_1/2D$, $G_2/1D \perp 1D$, $G_2/2D\text{-}2D$, and $G_3/2D\text{-}2D\text{-}2D$ patterns with the classification precisions of 100%, 100%, 93%, 97%, and 96%, respectively (Figure S21). Such precision could be further increased by inputting more data according to the training progress (Figure S22). The trained DL model was employed at Step I to pre-categorize the 2DM anticounterfeiting patterns.

At Step II, a direct search-and-compare algorithm was employed to finally validate the 2DM pattern within the subgroup, where the SSIM[43] was chosen as the criterion (see detailed SSIM calculation in Supplemental Experimental Procedures). Through cross-comparison of 1,760 2DM patterns, the resulting SSIM distributions are presented in Figure 5B, based on which the SSIM thresholds were set at 0.37, 0.06, 0.08, 0.07, and 0.23 for $G_1/1D$, $G_1/2D$, $G_2/1D \perp 1D$, $G_2/2D\text{-}2D$, and $G_3/2D\text{-}2D\text{-}2D$ categories (see Supplemental Experimental Procedures), respectively, leading to 100% validation precision for all categories at Step II (Figure S21). With the trained DL model for classification and the preset SSIM thresholds for validation, Figure 5C demonstrates several typical scenarios for the two-step authentication mechanism. Figure 5Ci shows that a $G_2/2D\text{-}1D$ HQ image was tested into the software, which did not belong to any of the five categories and thus failed at the classification step (FAKE). In Figure 5Cii, a random $G_2/2D\text{-}2D$ HQ image, although classified into the $G_2/2D\text{-}2D$ category, failed at the second validation step as it was not in the database (FAKE). As one authentic $G_3/2D\text{-}2D\text{-}2D$ tag was examined (Figure 5Ciii), its HQ image passed both classification and validation steps (with SSIM of 1.0 and authenticated as REAL). With the CNN-based DL models trained with the LQ images at different contrast, brightness, focuses, and rotations, our *DeepKey* software demonstrated outstanding and adaptive capabilities of authenticating the captured LQ SEM images (Figure 5Civ), whereby a $G_2/1D\text{-}1D$ tag taken under poor brightness/contrast and focus conditions was still validated as REAL (with low SSIM of 0.43). The screenshots of authentication results under these scenarios are supplied in Figure S23. The two-step authentication ensured *m* times faster processing speed than conventional direct search-and-compare validation (*m* is the number of categories,

CellPress
OPEN ACCESS

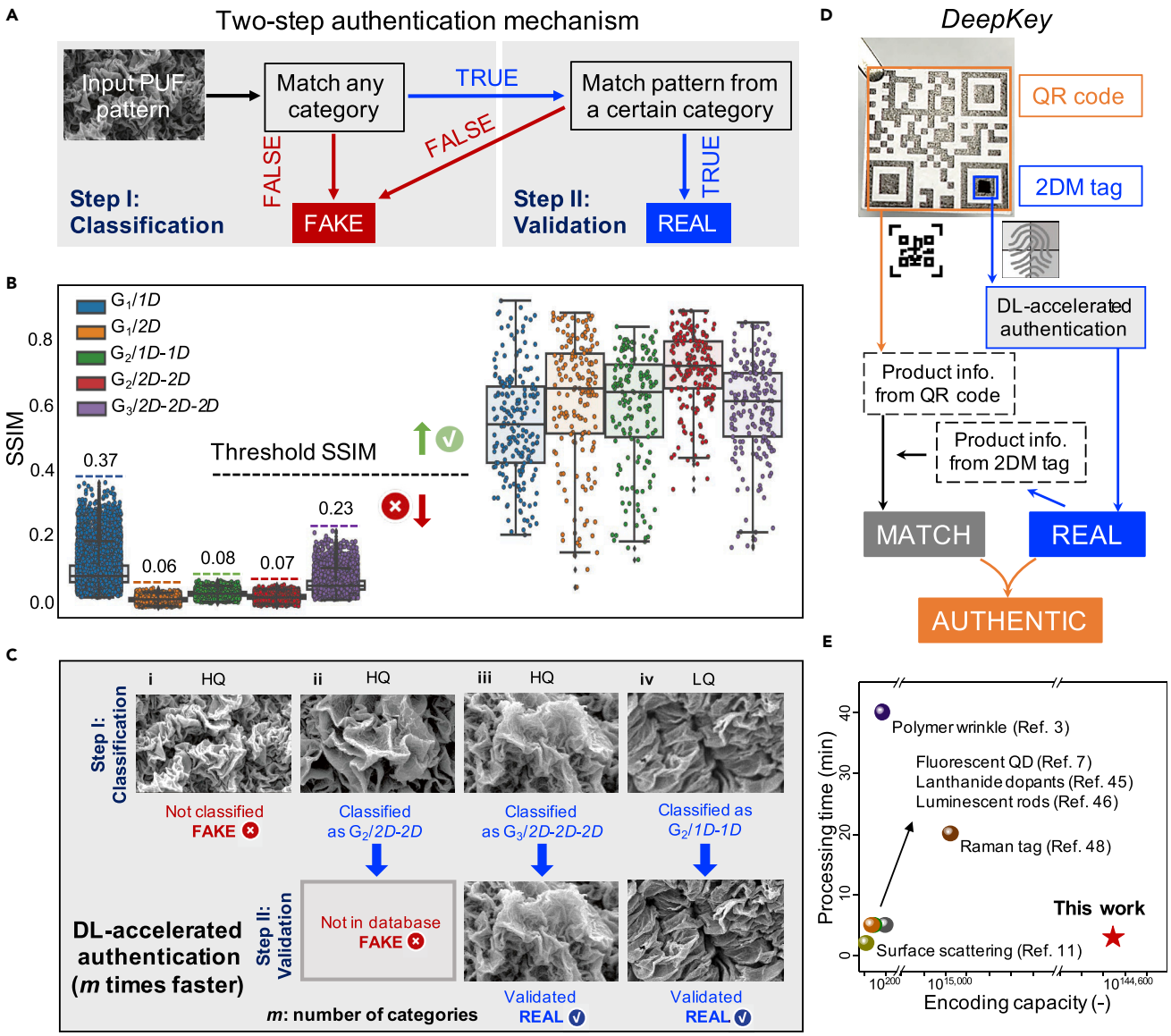

Figure 5. Synergy between Classifiable Two-Dimensional Material PUF Patterns and Deep Learning-Accelerated Authentication Mechanism Enabled the Development of *DeepKey* Anticounterfeiting Technology

(A) A two-step authentication mechanism, involving classification (Step I) and validation (Step II), was developed to accelerate the overall authentication process. Step I was used to classify the input PUF pattern (via deep learning [DL] model), and Step II was used to conduct the pattern validation within a narrowed, specific database (via search-and-compare algorithm).

(B) Box plot representing the SSIM distributions for REAL and FAKE PUF patterns, which were calculated based on the practical application scenarios. To avoid any "false-positive" validation, we set the threshold SSIM values at 0.37, 0.06, 0.08, 0.07, and 0.23 for $G_1/1D$, $G_1/2D$, $G_2/1D \perp 1D$, $G_2/2D$-$2D$, and $G_3/2D$-$2D$-$2D$ categories, respectively, to differentiate REAL and FAKE cases.

(C) Typical scenarios for the two-step authentication mechanism consisting of DL-accelerated classification and validation: (i) HQ PUF pattern that was not in any categories (FAKE), (ii) HQ PUF pattern that was classified into one category yet failed pattern validation (FAKE), (iii) HQ PUF pattern that passed both classification and validation (REAL, with SSIM of 1.00), and (iv) LQ PUF pattern (out of focus) that passed both classification and validation (REAL, with SSIM of 0.43).

(D) Two layers of information security in a *DeepKey* anticounterfeiting tag consisting of a two-dimensional material PUF pattern attached to a QR code (both were encoded with product information). Only when the PUF pattern was verified to be REAL by the *DeepKey* authentication software and the revealed product information matched that from the QR code was this product confirmed as AUTHENTIC, preventing the case of reusing the old anticounterfeiting tag.

(E) Our *DeepKey* technology demonstrated far higher encoding capacity and shorter processing time (verified by Video S1) compared with state-of-the-art systems.

as summarized in Figure S24), which significantly saves the overall authentication time especially when the database is huge. This is supported by the screenshots of self-developed *DeepKey* authentication software running the authentication of representative PUF patterns (Figure S25). It can be concluded that this DL-accelerated classification-and-validation strategy helps to break the trade-off between high encoding capacity (i.e., large database size) and long authentication time for most of the PUF-key-based anticounterfeiting systems. In addition, this authentication also ensures zero "false-positive" case (i.e., FAKE pattern is misauthenticated) in the database of 1,760 PUF patterns. Nevertheless, 2.9% "false-negative" cases (i.e., TRUE pattern fails the authentication) may occur due to low image quality (Supplemental Experimental Procedures), which can be resolved by taking multiple images during practical authentications.

DeepKey Technology Demonstrates High Encoding Capacity and Fast Authentication

The high-encoding-capacity 2DM tags can be further integrated with other information-encoding technologies to serve as an additional security layer. As shown in Figures 5D and S26, a QR code (blue box) was used as the first security layer to store the product information, which was read by an optical camera and retrieved by our self-developed *DeepKey* software. A MXene tag (2×2 mm^2, yellow box) was attached onto the bottom right corner of a QR code and served as a covert security layer to further authenticate the product information. The MXene PUF pattern was then captured by a benchtop SEM, which was then synced and examined by the *DeepKey* software. Only when the MXene PUF pattern is confirmed to be REAL (passes both classification and validation steps) will the product information be revealed by the *DeepKey* software. On top of that, only when the information retrieved from QR code and PUF pattern are identical will the product be confirmed as AUTHENTIC. Any other case will be suspected as COUNTERFEIT. As shown in Video S1, the overall processing time for *DeepKey* technology (SEM readout + data sync + authentication) was verified to be 3.5 min, compared with the 2–40 min estimated for other PUF systems without real demonstrations (Figure 5E).[1] Combined with its superior encoding capacity of $\sim 10^{144,494}$, our *DeepKey* technology breaks the long-standing trade-off between high encoding capacity and long authentication time for most of the PUF-key-based anticounterfeiting systems.

Conclusion

To conclude, we developed scalable, programmable, and generalized fabrication approaches for the creation of multigenerational topographies of GO and MXene by applying intermediate treatments between sequential substrate contractions. The intermediate CI and MIL treatments were developed to *in situ* adjust the mechanical mismatch and weaken the adhesion energy of 2DM/latex interface, respectively, enabling programmable topographic control in a transfer-free fashion. Together with the utilization of both sphere- and tube-shaped balloons, libraries of 2DM topographies were constructed by following user-designated deflation sequences with intermediate CI and/or MIL treatments implemented. The multigenerational 2DM patterns with high-level characteristics were next applied as the PUF-based secure keys for anticounterfeiting. Benefiting from the fast SEM image capture (readout) and the DL-facilitated authentication mechanism, the total processing time was significantly shortened (<3.5 min) without sacrificing its encoding capacity ($>10^{144,494}$) and anticounterfeiting reliability (i.e., zero "false-positive" case). Our anticounterfeiting technology, *DeepKey*, further introduced the use of a 2DM pattern as an add-on covert layer for conventional information security techniques (e.g., QR code).

CellPress
OPEN ACCESS

In particular, we would like to highlight our *in situ* approach of fabricating multigenerational 2DM topographies along sequential balloon deflations, in contrast to traditional approaches of using polystyrene shrink film as substrates.[18,26,34] Several significant advantages are summarized as follows. First, both CI and MIL intermediate treatments can be conducted in a transfer-free fashion, without the need of any troublesome substrate dissolvation or delicate 2DM thin film transfer required by the conventional approach for obtaining higher-generational topographies. Second, for our approach, the type (i.e., anisotropic 1D wrinkle, isotropic 2D crumple) and size of characteristic feature formed at each generation can be easily tuned by varying the deformation type (i.e., uniaxial and biaxial contraction) and pre-applied strain of substrate, by controlling the deflation program (i.e., direction and volume of deflation) at each stage and shape (i.e., sphere- and tube-shaped) of the latex balloon. For the conventional approach, however, the default deformation type (i.e., biaxial contraction) and pre-applied strain (i.e., areal strain of 300%) cannot be easily altered. Third, the conventional approach involves harsh treatments such as thermal-induced shrinkage and substrate dissolvation in organic solvents (e.g., dichloromethane), while our approach only has exposure to gentle salt solution or low temperature. In other words, our strategy allows the fabrication of multigenerational 2DM (other thin films may also apply) hierarchies with theoretically unlimited programmability and complexity in a facile, versatile, scalable, and gentle approach.

EXPERIMENTAL PROCEDURES

Resource Availability

Lead Contact

Further information and requests for resources and reagents should be directed to and will be fulfilled by the Lead Contact, Po-Yen Chen (checp@umd.edu).

Materials Availability

This study did not generate new unique reagents.

Data and Code Availability

All data needed to evaluate the conclusions in the paper are presented in the paper and/or Supplemental Information. Source code of self-developed *DeepKey* authentication software has been deposited to Mendeley Data: DOI: https://doi.org/10.17632/ZW37WSCRFN.1. Additional data related to this paper may be requested from the authors.

Details regarding materials and experimental procedures are provided in Supplemental Information.

Materials

Lithium fluoride (LiF, Sigma-Aldrich, BioUltra, ≥99.0%), hydrochloric acid (HCl, Sigma-Aldrich, ACS reagent, 37%), aluminum nitrate nonahydrate ($Al(NO_3)_3 \cdot 9H_2O$, Sigma-Aldrich, ACS reagent, ≥98%), Ti_3AlC_2 MAX powders (MAX, Tongrun Info Technology, China), ethanol (Thermo Fisher, >99.5%), and graphene oxide (GO) aqueous dispersion (Angstron Materials, 5 mg mL^{-1}) were used as received without further purification. The latex balloons (Aihua Balloons, Hebei, China) were used after cleaning with ethanol. Deionized (DI) water (18.2 MΩ) was obtained from a Milli-Q water purification system (Millipore, Bedford, MA, USA) and used as water source throughout the work.

Preparation of $Ti_3C_2T_x$ MXene Nanosheets

$Ti_3C_2T_x$ MXene nanosheets were prepared according to the literature with some modifications.[34] LiF (3.0 g) was added to 9.0 M HCl aqueous solution (40 mL) under

vigorous stirring. After the dissolution of LiF, 1.0 g of Ti_3AlC_2 MAX powders was slowly added into the solution. The mixture was then kept at 36°C for 24 h. Thereafter, the solid residue was washed with 2.0 M HCl solution (three times) and DI water (five times) until the pH value reached 7.0. Subsequently, the washed residue was added into 30 mL of DI water, ultrasonicated for 30 min, and centrifuged at 3,000 rpm for 20 min. The supernatant was finally collected as the final suspension of $Ti_3C_2T_x$ MXene nanosheets, and the concentration of MXene suspension was about 20 mg mL^{-1}. Further dilution was applied upon specific request.

Cation Intercalation Treatment

Taking GO as an example, a 500-nm-thick GO thin film with a diameter of 35 mm was first prepared by filtering 1 mL of 0.5 mg mL^{-1} GO aqueous dispersion through a hydrophobic polyvinylidene fluoride (PVDF) membrane (0.22 μm pore size, Merck Millipore). The air-dried GO thin film was then cut into specific dimensions, detached from PVDF membrane in ethanol, and transferred onto the plasma-treated latex balloon with specific inflation volumes. After evaporation of ethanol, the GO-coated latex balloon was immersed in 0.1 M $Al(NO_3)_3$ aqueous solution overnight followed by rinsing with DI water. Upon further drying, the Al^{3+}-intercalated GO (Al-GO) film on latex balloon underwent the specific sequence of subsequent deflation(s) to achieve the Al-GO crumples.

Moisture-Induced Lubrication Treatment

Taking MXene as an example, a 500-nm-thick MXene thin film with a diameter of 35 mm was first prepared by filtering 1 mL of 1.6 mg mL^{-1} MXene aqueous dispersion through the PVDF membrane. The dried MXene thin film was then cut into specific dimensions, detached from PVDF membrane in ethanol, and transferred onto the plasma-treated latex balloon with specific inflation volume. Thereafter, the MXene-coated latex balloon was kept at low temperature overnight, which was then taken out into the environment at room temperature and at RH of 68% to condense the moisture layer between the top MXene layer and the bottom latex substrate. After the MIL treatment, the MXene-coated latex balloon finally underwent the specific sequence of deflation(s) to achieve the MXene buckles with larger feature size. The temperature of MIL treatment could be varied to control the degree of delaminated buckling for tuning of the resulting feature size. In this work, temperatures of 4°C and −80°C were chosen for the intermediate MIL treatments for the generation of G_2 and G_3 topographies, respectively, whereby the latter (−80°C) resulted in larger feature size.

Programmable Architecturing of Multigenerational Two-Dimensional Material Topographies

For the fabrication of multigenerational GO topographies, both CI and MIL treatments were involved. Both sphere- and tube-shaped balloons were adopted, while the tube-shaped balloon was specifically required to encode *1D* wrinkle feature. To obtain G_1 topographies, we applied CI, MIL, or no additional treatment up to the requirement of ultimate patterns. To achieve G_2 topographies, we applied either CI or MIL (at 4°C) treatment between the first and second deflations. For fabrication of G_3 topographies, two routes were valid: (1) apply CI and MIL (at −80°C) treatments between the first-to-second and second-to-third deflations, respectively; (2) apply two MIL treatments (at 4°C and at −80°C) between the first-to-second and second-to-third deflations, respectively.

For fabrication of the MXene multigenerational topographies, MIL treatment was adopted during the sequential deflations of a MXene-coated inflated balloon.

Both sphere- and tube-shaped balloons were adopted, while the tube-shaped balloon was specifically required to encode *1D* wrinkle feature. To obtain G_1 topographies, we applied MIL or no additional treatment up to the requirement of ultimate patterns. To achieve G_2 topographies, we applied MIL (at 4°C) treatment between the first and second deflations. To fabricate G_3 topographies, we applied MIL treatments (at 4°C and at −80°C) between the first-to-second and second-to-third deflations, respectively.

2D crumple features were obtained by conducting the isotropic deflation of either sphere- or tube-shaped balloons as elastomeric substrates, while *1D* wrinkle features were obtained by undergoing *1D* anisotropic deflation of tube-shaped balloons. The diverse characteristics of hierarchical 2DM topographies, including hierarchical level, feature size, feature type, and deformation sequences, could be programmably tuned by adjusting various fabrication parameters, such as numbers of deflation stages, $\Delta\varepsilon_A/\Delta\varepsilon$ at each deflation stage, and directions and sequences of deflations.

To achieve final 2DM hierarchical topographies with similar macroscopic dimensions (~1.0 × 1.0 cm^2), we adopted thin films with dimensions of ~1.8 × 1.8, 2.2 × 2.2, and 2.6 × 2.6 cm^2 for the fabrication of G_1, G_2, and G_3 topographies, respectively, for which a sphere-shaped balloon with diameter of 2.0 cm (deflated) was used. The tube-shaped balloon used here had length and width of 10.0 cm and 1.0 cm (deflated), respectively.

Regarding the multigenerational GO and MXene topographies presented in Figure 4, the specific fabrication routes are listed below.

GO Genealogy

G_1/*2D*: One-stage full deflation with $\Delta\varepsilon_A$ of 200% (volume change: 30 to 0 mL); both sphere- and tube-shaped balloons could be applied.

G_1/*1D*: One-stage full relaxation with $\Delta\varepsilon$ of 100%; tube-shaped balloon was applied with uniaxial relaxation along its axis direction.

G_2/*2D-2D*: Two-stage deflations of 200% to 200% ($\Delta\varepsilon_A$ at first stage to $\Delta\varepsilon_A$ at second stage; volume changes: 60 to 30 mL to 30 to 0 mL); both sphere- and tube-shaped balloons could be applied; CI treatment was applied between the first and second deflations.

G_2/*2D-1D*: Two-stage deformations of 200% to 100% ($\Delta\varepsilon_A$ at first stage to $\Delta\varepsilon$ at second stage; volume change: 30 to 0 mL for first stage); tube-shaped balloon was applied for the second-stage uniaxial relaxation along its axis direction; CI treatment was applied between the first and second deformations.

G_2/*1D-2D*: Two-stage deformations of 100% to 200% ($\Delta\varepsilon$ at first stage to $\Delta\varepsilon_A$ at second stage; volume change: 30 to 0 mL for second stage); tube-shaped balloon was applied for the first-stage uniaxial relaxation vertical to its axis direction; CI treatment was applied between the first and second deformations.

G_2/*1D*⊥*1D*: Two-stage deformations of 100% to 100% ($\Delta\varepsilon$ at first stage to $\Delta\varepsilon$ at second stage); tube-shaped balloon was applied for the first-stage uniaxial relaxation vertical to its axis direction and the second-stage uniaxial relaxation along its axis direction; CI treatment was applied between the first and second deformations.

G_3/*2D-2D-2D*: Three-stage deflations of 200% to 200% to 200% ($\Delta\varepsilon_A$ at first stage to $\Delta\varepsilon_A$ at second stage to $\Delta\varepsilon_A$ at third stage; volume changes: 90 to 60 mL, to 60 to 30 mL, to 30 to 0 mL); both sphere- and tube-shaped balloons could be applied; CI and MIL (at −80°C) treatments were applied between the first and second and between the second and third deflations, respectively.

G_3/*2D-1D-2D*: Three-stage deformations of 200% to 100% to 200% ($\Delta\varepsilon_A$ at first stage to $\Delta\varepsilon$ at second stage to $\Delta\varepsilon_A$ at third stage; volume changes: 60 to 30 mL for first stage, 30 to 0 mL for third stage); tube-shaped balloon was applied for the second-stage uniaxial relaxation vertical to its axis direction; CI and MIL (at −80°C) treatments were applied between the first and second and between the second and third deformations, respectively.

G_3/*2D-1D⊥1D*: Three-stage deformations of 200% to 100% to 100% ($\Delta\varepsilon_A$ at first stage to $\Delta\varepsilon$ at second stage to $\Delta\varepsilon$ at third stage; volume change: 30 to 0 mL for first stage); tube-shaped balloon was applied for the second-stage uniaxial relaxation vertical to its axis direction and the third-stage uniaxial relaxation along its axis direction; CI and MIL (at −80°C) treatments were applied between the first and second and between the second and third deformations, respectively.

G_3/*1D||1D-2D*: Three-stage deformations of 100% to 100% to 200% ($\Delta\varepsilon$ at first stage to $\Delta\varepsilon$ at second stage to $\Delta\varepsilon_A$ at third stage; volume change: 30 to 0 mL for third stage); tube-shaped balloon was applied for the first- and second-stage uniaxial relaxations along its axis direction; CI and MIL (at −80°C) treatments were applied between the first and second and between the second and third deformations, respectively.

MXene Genealogy

G_1/*2D*: One-stage full deflation with $\Delta\varepsilon_A$ of 200% (volume change: 30 to 0 mL); both sphere- and tube-shaped balloons could be applied.

G_1/*1D*: One-stage full relaxation with $\Delta\varepsilon$ of 100%; tube-shaped balloon was applied with uniaxial relaxation along its axis direction.

G_2/*2D-2D*: Two-stage deflations of 200% to 200% ($\Delta\varepsilon_A$ at first stage to $\Delta\varepsilon_A$ at second stage; volume changes: 60 to 30 mL to 30 to 0 mL); both sphere- and tube-shaped balloons could be applied; MIL treatment was applied between the first and second deflations.

G_2/*2D-1D*: Two-stage deformations of 200% to 100% ($\Delta\varepsilon_A$ at first stage to $\Delta\varepsilon$ at second stage; volume change: 30 to 0 mL for first stage); tube-shaped balloon was applied for the second-stage uniaxial relaxation along its axis direction; MIL treatment was applied between the first and second deformations.

G_2/*1D-2D*: Two-stage deformations of 100% to 200% ($\Delta\varepsilon$ at first stage to $\Delta\varepsilon_A$ at second stage; volume change: 30 to 0 mL for second stage); tube-shaped balloon was applied for the first-stage uniaxial relaxation vertical to its axis direction; MIL treatment was applied between the first and second deformations.

G_2/*1D⊥1D*: Two-stage deformations of 100% to 100% ($\Delta\varepsilon$ at first step to $\Delta\varepsilon$ at second step); tube-shaped balloon was applied for the first-stage uniaxial relaxation vertical to its axis direction and the second-stage uniaxial relaxation along its axis direction; MIL treatment was applied between the first and second deformations.

G_3/*2D-2D-2D*: Three-stage deflations of 200% to 200% to 200% ($\Delta\varepsilon_A$ at first stage to $\Delta\varepsilon_A$ at second stage to $\Delta\varepsilon_A$ at third stage; volume changes: 90 to 60 mL, to 60 to 30 mL, to 30 to 0 mL); both sphere- and tube-shaped balloons could be applied; MIL treatments (at 4°C and at −80°C) were applied between the first and second and between the second and third deflations, respectively.

G_3/*2D-2D-1D*: Three-stage deformations of 200% to 200% to 100% ($\Delta\varepsilon_A$ at first stage to $\Delta\varepsilon_A$ at second stage to $\Delta\varepsilon$ at third stage; volume changes: 60 to 30 mL for first stage, 30 to 0 mL for second stage); tube-shaped balloon was applied for the third-stage uniaxial relaxation along its axis direction; MIL treatments (at 4°C and at −80°C) were applied between the first and second and between the second and third deformations, respectively.

G_3/*2D-1D-2D*: Three-stage deformations of 200% to 100% to 200% ($\Delta\varepsilon_A$ at first stage to $\Delta\varepsilon$ at second stage to $\Delta\varepsilon_A$ at third stage; volume changes: 60 to 30 mL for first stage, 30 to 0 mL for third stage); tube-shaped balloon was applied for the second-stage uniaxial relaxation vertical to its axis direction; MIL treatments (at 4°C and at −80°C) were applied between the first and second and between the second and third deformations, respectively.

G_3/*1D-2D-1D*: Three-stage deformations of 100% to 200% to 100% ($\Delta\varepsilon$ at first stage to $\Delta\varepsilon_A$ at second stage to $\Delta\varepsilon$ at third stage; volume change: 30 to 0 mL for second stage); tube-shaped balloon was applied for the first-stage uniaxial relaxation vertical to its axis direction and the third-stage uniaxial relaxation along its axis direction; MIL treatments (at 4°C and at −80°C) were applied between the first and second and between the second and third deformations, respectively.

Environmental Stability Tests

The G_1/*2D* GO and MXene PUF patterns were characterized by SEM before and after their exposures to various harsh treatments, the details of which are depicted as follows.

Organic solvent immersion: the G_1/*2D* GO and MXene PUF patterns were fully immersed in dichloromethane (DCM) for 1 min to simulate the DCM spill. The SEM images before and after the treatment were respectively taken for comparison.

UV light illumination: the G_1/*2D* GO and MXene PUF patterns were exposed to UV light with wavelength of 254 nm and energy density of 0.12 J cm^{-2} for 60 min, which were conducted within the chamber of SPECRTROLINKER (XL-1500 UV CROSSLINKER).

Strong acid immersion: the G_1/*2D* GO and MXene PUF patterns were fully immersed in 6.0 M HCl (pH −0.78) for 60 s to simulate the acid spill.

Strong base immersion: the G_1/*2D* GO and MXene PUF patterns were fully immersed in 6.0 M NaOH (pH 14.78) for 60 s to simulate the base spill.

Low temperature: the G_1/*2D* GO and MXene PUF patterns were put into the fridge at −20°C for 60 min.

High temperature: the G_1/*2D* GO and MXene PUF patterns were put into the oven at 150°C for 3 min.

Low humidity: the $G_1/2D$ GO and MXene PUF patterns were put into the sealed desiccator with 0% RH for 12 h. The RH was controlled using desiccant-silica gel and monitored using hygrometer.

High humidity: the $G_1/2D$ GO and MXene PUF patterns were put into the sealed desiccator with 90% RH for 12 h. The sealed desiccator was humidified with the cotton balls wetted by warm water. The RH was monitored by a hygrometer.

Long-term stabilities: the $G_1/2D$ GO and MXene PUF patterns were exposed to daylight (25°C, RH 68%) for 30 days.

Characterization

The surface morphologies of multigenerational GO and MXene topographies and their cross-section information were obtained by using a scanning electron microscope (FEI Quanta 600), a benchtop scanning electron microscope (JCM-7000 NeoScope Benchtop), and a field-emission scanning electron microscope (JEOL-JSM-6610LV) operated at 15.0 kV. The as-prepared MXene and as-received GO nanosheets were characterized by using a high-resolution transmission electron microscope (JEOL 2010F). XRD patterns were recorded by an X-ray diffractometer (Bruker, D8 Advance X-ray Powder Diffractometer, Cu Kα [λ = 0.154 nm] radiation) with a scan rate of 2° min^{-1}. Uniaxial tensile tests and delamination tests were conducted by using a Universal Testing System (Instron 5567; Instron, Canton, MA) at room temperature with a 500-N load cell. Detailed descriptions of the delamination tests can be found in Supplemental Experimental Procedures. X-ray photoelectron spectroscopy was conducted by a Kratos AXIS Ultra^{DLD} instrument by using a microfocused (100 μm, 25 W) Al X-ray beam with a photoelectron take-off angle of 90°. Raman spectra were obtained using a Raman microscope (XploRA ONETM, Horiba) for which 638-nm and 785-nm lasers were adopted for GO and MXene, respectively.

Convolutional Neural Network Deep Learning

Based on the Pytorch library, a CNN DL model was built to classify the PUF patterns of 2DM tags. The network consisted of one input layer (PUF pattern), three convolutional layers, three max-pooling (MP) layers, one fully connected (FC) layer, and one output layer (classification model). The output of the last FC layer produced a distribution of five class labels ($G_1/1D$, $G_1/2D$, $G_2/1D \perp 1D$, $G_2/2D\text{-}2D$, and $G_3/2D\text{-}2D\text{-}2D$). The first convolutional layer filtered the 300 × 200 × 3 input image with eight kernels of size 5 × 5 × 3 with a stride of 1 pixel, and an MP layer with a kernel of size 5 was used to filter its output. The second convolutional layer took the output from the first layer as input and filtered it with 16 kernels of size 5 × 5 × 16, and an MP layer with a kernel of size 2 was used to filter its output. The third convolutional layer possessed 32 kernels of size 5 × 5 × 32 connected to the output from the second layer, and after the filter of a 5 × 5 MP layer, the output of the third layer was connected to the last layer, the FC layer, which possessed 32 × 6 × 4 neurons and five linear outputs. NVIDIA Quadro P2000 was used to conduct the calculations.

SUPPLEMENTAL INFORMATION

Supplemental Information can be found online at https://doi.org/10.1016/j.matt.2020.10.005.

ACKNOWLEDGMENTS

The authors acknowledge the financial support provided by the Faculty Research Committee Start-Up grant of the National University of Singapore R-279-000-515-133; the

Ministry of Education Academic Research Fund R-279-000-532-114, R-279-000-551-114, and R-279-000-579-112; the AME Programmatic grant R-279-000-560-305 (A*STAR grant no. A1898b0043); the AME Young Investigator Research grant R-279-000-546-305 (A*STAR grant no. A1884c0017); and the Singapore-MIT Alliance for Research and Technology Ignition grant R-279-000-572-592. P-.Y.C. also acknowledges the Start-Up fund of the University of Maryland, College Park.

AUTHOR CONTRIBUTIONS

Conceptualization, L.J., P.-Y.C., Q.X., X.W., and H.Y.; Investigation, L.J., Q.X., H.L., K.L., P.L.P.N., S.L., and Y.L.; Resources, E.H.T.T.; Data Curation, L.J. and Q.X.; Writing – Original Draft, L.J.; Writing – Review & Editing, P.-Y.C., Q.X., and X.W.; Supervision, P.-Y.C. and X.W.; Project Administration, P.-Y.C. and X.W.; Funding Acquisition, P.-Y.C. and X.W.

DECLARATION OF INTERESTS

The authors declare no competing interests.

Received: May 26, 2020
Revised: August 25, 2020
Accepted: October 2, 2020
Published: November 2, 2020

REFERENCES

1. Arppe, R., and Sørensen, T.J. (2017). Physical unclonable functions generated through chemical methods for anti-counterfeiting. Nat. Rev. Chem. *1*, 0031.
2. Kim, J., Yun, J.M., Jung, J., Song, H., Kim, J.-B., and Ihee, H. (2014). Anti-counterfeit nanoscale fingerprints based on randomly distributed nanowires. Nanotechnology *25*, 155303.
3. Bae, H.J., Bae, S., Park, C., Han, S., Kim, J., Kim, L.N., Kim, K., Song, S.-H., Park, W., and Kwon, S. (2015). Biomimetic microfingerprints for anti-counterfeiting strategies. Adv. Mater. *27*, 2083–2089.
4. Smith, A.F., Patton, P., and Skrabalak, S.E. (2016). Plasmonic nanoparticles as a physically unclonable function for responsive anti-counterfeit nanofingerprints. Adv. Funct. Mater. *26*, 1315–1321.
5. Hu, Z., Comeras, J.M.M.L., Park, H., Tang, J., Afzali, A., Tulevski, G.S., Hannon, J.B., Liehr, M., and Han, S.-J. (2016). Physically unclonable cryptographic primitives using self-assembled carbon nanotubes. Nat. Nanotechnol. *11*, 559–565.
6. Moon, D.-I., Rukhin, A., Gandhiraman, R.P., Kim, B., Kim, S., Seol, M.-L., Yoon, K.J., Lee, D., Koehne, J., Han, J.-W., et al. (2019). Physically unclonable function by an all-printed carbon nanotube network. ACS Appl. Electron. Mater. *1*, 1162–1168.
7. Liu, Y., Han, F., Li, F., Zhao, Y., Chen, M., Xu, Z., Zheng, X., Hu, H., Yao, J., Guo, T., et al. (2019). Inkjet-printed unclonable quantum dot fluorescent anti-counterfeiting labels with artificial intelligence authentication. Nat. Commun. *10*, 2409.
8. Nam, H., Song, K., Ha, D., and Kim, T. (2016). Inkjet printing based mono-layered photonic crystal patterning for anti-counterfeiting structural colors. Sci. Rep. *6*, 30885.
9. Cui, Y., Phang, I.Y., Lee, Y.H., Lee, M.R., Zhang, Q., and Ling, X.Y. (2015). Multiplex plasmonic anti-counterfeiting security labels based on surface-enhanced Raman scattering. Chem. Commun. *51*, 5363–5366.
10. Wolterink, T.A.W., Uppu, R., Ctistis, G., Vos, W.L., Boller, K.-J., and Pinkse, P.W.H. (2016). Programmable two-photon quantum interference in 103 channels in opaque scattering media. Phys. Rev. A *93*, 053817.
11. Cowburn, R. (2008). Laser surface authentication—reading Nature's own security code. Contemp. Phys. *49*, 331–342.
12. Glover, A., Aziz, N., Pillmoor, J., McCallien, D.W.J., and Croud, V.B. (2011). Evaluation of DNA as a taggant for fuels. Fuel *90*, 2142–2146.
13. Gooch, J., Goh, H., Daniel, B., Abbate, V., and Frascione, N. (2016). Monitoring criminal activity through invisible fluorescent "peptide coding" taggants. Anal. Chem. *88*, 4456–4460.
14. Duong, B., Liu, H., Li, C., Deng, W., Ma, L., and Su, M. (2014). Printed multilayer microtaggants with phase change nanoparticles for enhanced labeling security. ACS Appl. Mater. Interfaces *6*, 8909–8912.
15. Johansen, S., Radziwon, M., Tavares, L., and Rubahn, H.-G. (2012). Nanotag luminescent fingerprint anti-counterfeiting technology. Nanoscale Res. Lett. *7*, 262.
16. Radziwon, M., Johansen, S., and Rubahn, H.-G. (2014). Anti-counterfeit solution from organic semiconductor. Procedia Eng. *69*, 1405–1409.
17. Geng, Y., Noh, J., Drevensek-Olenik, I., Rupp, R., Lenzini, G., and Lagerwall, J.P.F. (2016). High-fidelity spherical cholesteric liquid crystal Bragg reflectors generating unclonable patterns for secure authentication. Sci. Rep. *6*, 26840.
18. Chen, P.-Y., Sodhi, J., Qiu, Y., Valentin, T.M., Steinberg, R.S., Wang, Z., Hurt, R.H., and Wong, I.Y. (2016). Multiscale graphene topographies programmed by sequential mechanical deformation. Adv. Mater. *28*, 3564–3571.
19. Lee, W.-K., and Odom, T.W. (2019). Designing hierarchical nanostructures from conformable and deformable thin materials. ACS Nano *13*, 6170–6177.
20. Jing, L., Li, K., Yang, H., and Chen, P.-Y. (2020). Recent advances in integration of 2D materials with soft matter for multifunctional robotic materials. Mater. Horiz. *7*, 54–70.
21. Tian, L., Liu, K.-K., Fei, M., Tadepalli, S., Cao, S., Geldmeier, J.A., Tsukruk, V.V., and Singamaneni, S. (2016). Plasmonic nanogels for unclonable optical tagging. ACS Appl. Mater. Interfaces *8*, 4031–4041.
22. Perreault, F., Fonseca de Faria, A., and Elimelech, M. (2015). Environmental applications of graphene-based nanomaterials. Chem. Soc. Rev. *44*, 5861–5896.
23. Bae, H.J., Bae, S., Yoon, J., Park, C., Kim, K., Kwon, S., and Park, W. (2017). Self-organization of maze-like structures via guided wrinkling. Sci. Adv. *3*, e1700071.
24. Chen, P.-Y., Liu, M., Wang, Z., Hurt, R.H., and Wong, I.Y. (2017). From flatland to spaceland: higher dimensional patterning with two-

dimensional materials. Adv. Mater. *29*, 1605096.

25. Lee, W.-K., Engel, C.J., Huntington, M.D., Hu, J., and Odom, T.W. (2015). Controlled three-dimensional hierarchical structuring by memory-based, sequential wrinkling. Nano Lett. *15*, 5624–5629.

26. Jung, W.-B., Cho, K.M., Lee, W.-K., Odom, T.W., and Jung, H.-T. (2018). Universal method for creating hierarchical wrinkles on thin-film surfaces. ACS Appl. Mater. Interfaces *10*, 1347–1355.

27. Huang, Z.Y., Hong, W., and Suo, Z. (2005). Nonlinear analyses of wrinkles in a film bonded to a compliant substrate. J. Mech. Phys. Solids *53*, 2101–2118.

28. Lin, H., Li, Y., and Zhu, J. (2020). Cross-linked GO membranes assembled with GO nanosheets of differently sized lateral dimensions for organic dye and chromium separation. J. Membr. Sci. *598*, 117789.

29. Medhekar, N.V., Ramasubramaniam, A., Ruoff, R.S., and Shenoy, V.B. (2010). Hydrogen bond networks in graphene oxide composite paper: structure and mechanical properties. ACS Nano *4*, 2300–2306.

30. Wan, J., Lacey, S.D., Dai, J., Bao, W., Fuhrer, M.S., and Hu, L. (2016). Tuning two-dimensional nanomaterials by intercalation: materials, properties and applications. Chem. Soc. Rev. *45*, 6742–6765.

31. Park, S., Lee, K.-S., Bozoklu, G., Cai, W., Nguyen, S.T., and Ruoff, R.S. (2008). Graphene oxide papers modified by divalent ions—enhancing mechanical properties via chemical cross-linking. ACS Nano *2*, 572–578.

32. Yeh, C.-N., Raidongia, K., Shao, J., Yang, Q.-H., and Huang, J. (2015). On the origin of the stability of graphene oxide membranes in water. Nat. Chem. *7*, 166.

33. Chang, T.-H., Tian, Y., Li, C., Gu, X., Li, K., Yang, H., Sanghani, P., Lim, C.M., Ren, H., and Chen, P.-Y. (2019). Stretchable graphene pressure sensors with Shar-Pei-like hierarchical wrinkles for collision-aware surgical robotics. ACS Appl. Mater. Interfaces *11*, 10226–10236.

34. Li, K., Chang, T.-H., Li, Z., Yang, H., Fu, F., Li, T., Ho, J.S., and Chen, P.-Y. (2019). Biomimetic MXene textures with enhanced light-to-heat conversion for solar steam generation and wearable thermal management. Adv. Energy Mater. *9*, 1901687.

35. Chen, P.-Y., Liu, M., Valentin, T.M., Wang, Z., Spitz Steinberg, R., Sodhi, J., Wong, I.Y., and Hurt, R.H. (2016). Hierarchical metal oxide topographies replicated from highly textured graphene oxide by intercalation templating. ACS Nano *10*, 10869–10879.

36. Hu, X., Dou, Y., Li, J., and Liu, Z. (2019). Buckled structures: fabrication and applications in wearable electronics. Small *15*, 1804805.

37. Nolte, A.J., Young Chung, J., Davis, C.S., and Stafford, C.M. (2017). Wrinkling-to-delamination transition in thin polymer films on compliant substrates. Soft Matter *13*, 7930–7937.

38. Li, S., Han, M., Rogers, J.A., Zhang, Y., Huang, Y., and Wang, H. (2019). Mechanics of buckled serpentine structures formed via mechanics-guided, deterministic three-dimensional assembly. J. Mech. Phys. Solids *125*, 736–748.

39. Zhang, Q., and Yin, J. (2018). Spontaneous buckling-driven periodic delamination of thin films on soft substrates under large compression. J. Mech. Phys. Solids *118*, 40–57.

40. Kim, D.-I., Ahn, H.-S., and Choi, D.-H. (2004). Effect of surface hydrophilicity and water vapor pressure on the interfacial shear strength of adsorbed water layer. Appl. Phys. Lett. *84*, 1919–1921.

41. Schumacher, A., Kruse, N., Prins, R., Meyer, E., Lüthi, R., Howald, L., Güntherodt, H.J., and Scandella, L. (1996). Influence of humidity on friction measurements of supported MoS_2 single layers. J. Vac. Sci. Technol. B *14*, 1264–1267.

42. Song, J., Tan, Y., Chu, Z., Xiao, M., Li, G., Jiang, Z., Wang, J., and Hu, T. (2019). Hierarchical reduced graphene oxide ridges for stretchable, wearable, and washable strain sensors. ACS Appl. Mater. Interfaces *11*, 1283–1293.

43. Wang, Z., and Bovik, A.C. (2009). Mean squared error: love it or leave it? A new look at Signal Fidelity Measures. IEEE Signal Process. Mag. *26*, 98–117.

44. Sood, B., Das, D., and Pecht, M. (2011). Screening for counterfeit electronic parts. J. Mater. Sci. Mater. Electron. *22*, 1511.

45. Carro-Temboury, M.R., Arppe, R., Vosch, T., and Sørensen, T.J. (2018). An optical authentication system based on imaging of excitation-selected lanthanide luminescence. Sci. Adv. *4*, e1701384.

46. Kumar, P., Dwivedi, J., and Gupta, B.K. (2014). Highly luminescent dual mode rare-earth nanorod assisted multi-stage excitable security ink for anti-counterfeiting applications. J. Mater. Chem. C *2*, 10468–10475.

47. Buchanan, J.D.R., Cowburn, R.P., Jausovec, A.-V., Petit, D., Seem, P., Xiong, G., Atkinson, D., Fenton, K., Allwood, D.A., and Bryan, M.T. (2005). 'Fingerprinting' documents and packaging. Nature *436*, 475.

48. Gu, Y., He, C., Zhang, Y., Lin, L., Thackray, B.D., and Ye, J. (2020). Gap-enhanced Raman tags for physically unclonable anticounterfeiting labels. Nat. Commun. *11*, 516.

49. Abdelmoula, W.M., Balluff, B., Englert, S., Dijkstra, J., Reinders, M.J.T., Walch, A., McDonnell, L.A., and Lelieveldt, B.P.F. (2016). Data-driven identification of prognostic tumor subpopulations using spatially mapped t-SNE of mass spectrometry imaging data. Proc. Natl. Acad. Sci. U S A *113*, 12244–12249.

50. Wong, M.T., Ong, D.E.H., Lim, F.S.H., Teng, K.W.W., McGovern, N., Narayanan, S., Ho, W.Q., Cerny, D., Tan, H.K.K., Anicete, R., et al. (2016). A high-dimensional atlas of human T cell diversity reveals tissue-specific trafficking and cytokine signatures. Immunity *45*, 442–456.

51. Kruiger, J.F., Rauber, P.E., Martins, R.M., Kerren, A., Kobourov, S., and Telea, A.C. (2017). Graph layouts by t-SNE. Comput. Graph. Forum *36*, 283–294.

52. Zeng, N., Zhang, H., Song, B., Liu, W., Li, Y., and Dobaie, A.M. (2018). Facial expression recognition via learning deep sparse autoencoders. Neurocomputing *273*, 643–649.

53. Gu, J., Wang, Z., Kuen, J., Ma, L., Shahroudy, A., Shuai, B., Liu, T., Wang, X., Wang, G., Cai, J., et al. (2018). Recent advances in convolutional neural networks. Pattern Recognit. *77*, 354–377.